

Viscous instability formation in a two-layer fluid

Emma Lepinay and Emily Chen *

Abstract The stability of a viscously-stratified two-layer fluid is investigated through experiments and a mathematical model. We first assess the instability pattern formation experimentally by oscillating a layer of viscous golden syrup covered by a less viscous water layer. A simple mathematical model of a single layer undergoing unidirectional shear stress is used to understand the onset of stability. The model predicts that the flow is stable under the experimental regime while the experiments show clear deformations.

1 The Honey Problem

As a promotional tactic, one honey vendor in the Queen Victoria market claims that their natural honey exhibits a “genetic memory” that distinguishes it from other honeys. To demonstrate this genetic memory, the vendor pours some honey into a dish, covers it with a layer of water, and shakes the dish. As a result of shaking, a pattern becomes visible in the honey layer—a pattern resembling a honeycomb (Fig. 1(a)). Hence, the vendor claims that the honey retains some form of memory of where it came from (i.e. the honeycombs comprising bees’ nests).

In this article, we set out to examine this pattern formation phenomenon induced by oscillating two horizontally-stratified fluid layers with different viscosities. We

Emma Lepinay
Institute of Energy and Environmental Flows, University of Cambridge, UK
e-mail: el547@cam.ac.uk

Emily Chen
Department of Chemical & Biological Engineering, Princeton University, USA
e-mail: ec2619@princeton.edu

* This report presents the results of a project, originally posed by Dr Draga Pihler-Puzović (University of Manchester), and undertaken by the authors at the Matrix Workshop *Instabilities in Porous Media*, April 3-23, 2024.

first conduct controlled experiments to understand the parameters that influence the instability formation, finding that the instability arises with other viscous fluids and thus debunking the myth of genetic memory in special honeys. We next construct a comparable mathematical model of the system by considering a single viscous layer undergoing constant shear. We use linear stability analysis to predict the conditions for instability to develop. We find that in the absence of a second layer, the flow is stable for the cases modeling the experimental parameters.

2 Experimental investigation: pattern formation in stratified golden syrup and water layers under imposed 1-D oscillatory flow

2.1 Pattern formation in fluid flow instabilities

Fluid instabilities can give rise to remarkable patterns under certain flow conditions. Similar honey-comb and columnar type patterns have been observed in standing Faraday waves in single-layer fluids undergoing vertical oscillations [14], oscillatory flow over granular beds mimicking flow at the sea floor [2, 3, 10], ripples and waves in flows down an inclined plane [9], and even magnetically-induced honeycombs in stratified ferrofluid-oil systems [1]. Whilst the patterns visually may look similar, the physical mechanisms driving the instability in these examples are different: vertical fluid inertia, secondary flows carrying grains of sand, Reynolds stresses, and differences in magnetic polarizability, respectively. For the honey problem, we hypothesize that the viscosity difference between the two fluids ultimately generates the instability [4], whereby for a large enough viscosity ratio, the shear stress exerted by the less viscous fluid on the more viscous fluid can cause the fluid interface to become unstable. Theoretical treatments of these types of viscosity-stratification instabilities have been examined previously: bounded 2-layer fluids of infinite thicknesses [7, 5], thick upper fluid and thin lower fluid [6], bounded Couette flow [11], frozen waves in 2 layers of bounded fluid flows with wall effects [12], bounded 2-layer fluids [15], and even 3-layer bounded fluids [8]. Our problem differs from these previous studies in that the honey problem has an oscillating bottom boundary and a free surface boundary condition for the top fluid. Note that both honey and golden syrup are Newtonian fluids.

2.2 Methods

To more rigorously examine the pattern formation in viscosity-stratified fluids, we develop a systematic experimental protocol to observe how the instability pattern depends on the parameters of shaking amplitude A , frequency ω , and layer thick-

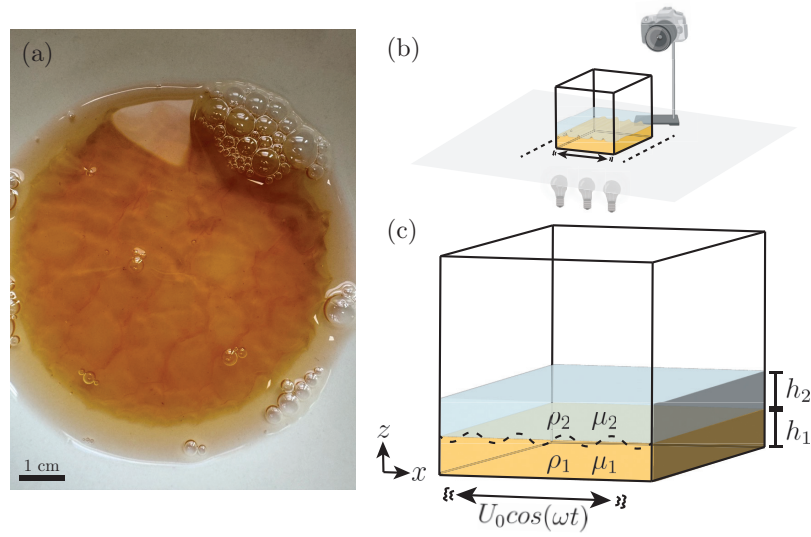


Fig. 1 Honey-water instability. (a) Image of instability pattern in honey after shaking with a layer of water on top. Here, shaking was applied in multiple directions. (b) Schematic of the experimental set-up. A container filled with the viscosity-stratified fluids is oscillated in a 1-D motion on a tabletop surface with lighting from below and imaging of the top surface from directly above. (c) Parameters in the honey problem.

ness ratio, h_w/h_h . We also switch our experimental viscous test fluid from honey to golden syrup for the viscous fluid layer as its rheological properties are well-established.

2.2.1 Test fluids

We use Lyle's golden syrup as the viscous fluid layer, which is a well-known Newtonian fluid with viscosity $\mu = 80 \text{ Pa s}$ and density $\rho = 1430 \text{ kg/m}^3$ at 20°C . We use water as the less viscous layer, with viscosity $\mu = 0.001 \text{ Pa s}$ and density $\rho = 998.2 \text{ kg/m}^3$ at 20°C . Thus, the viscosity ratio of the two fluids is $\mu_w/\mu_h = 1.2 \times 10^{-5}$, the density ratio is $\rho_w/\rho_h = 0.7$, and the kinematic viscosity ratio is $\nu_w/\nu_h = 1.8 \times 10^{-5}$.

2.2.2 Shaking protocol

We control the layer height thickness via the volume of fluid added to the transparent rectangular container of known cross-sectional area. For all experiments tested in this work, the layer height of the golden syrup is kept constant at $h_h = 0.5 \text{ cm}$. We explore layer height ratios over a range from $h_w/h_h = \frac{1}{3}$ – $\frac{4}{3}$, which corresponds

to water layer thicknesses of $h_w = 0.17\text{--}0.67$ cm. The water layer is gently syringed over the viscous layer to prevent any deformation of the interface, and the system is left to rest for 5 minutes before the experiment to allow for relaxation of the interface. Figure 1(b) depicts a schematic of the experimental set-up. The container is placed on top of a flat LED pad to improve imaging quality. A camera is propped directly overhead of the container to record videos during the shaking. Here, we manually shake the container in a side-to-side motion, whereby the displacement amplitude is marked on the surface, and the frequency is set by a metronome. We impose 2 minutes of shaking for each test condition, which was observed to be sufficiently long for the pattern to reach a pseudo-steady state (by eye) for this system. The experimental test frequencies range from $f = 1\text{--}2.1$ Hz (120–250 bpm), which we found to be near the experimental limit for accuracy in manually forcing the oscillations. All experiments are performed at room temperature. For all experiments, except the transient shaking experiments, we allow the system to relax back to equilibrium before commencing the next test condition.

2.2.3 Image and video processing

We extract images of the final pattern from the last frames of the recorded videos at each test condition. To improve the visualization of the pattern, we process the images in ImageJ by converting them to grayscale and enhancing the image contrast.

2.3 Results

2.3.1 Controls: single layer experiments

We first investigate each individual fluid's behavior under 1-D shaking separately at a fluid thickness of 5 mm. For oscillation of the water alone, we observe oscillating surface waves but no persistent pattern over the range of experimentally-tested frequencies. For oscillation of the golden syrup, we observe no visible surface deformation, presumably due to the extremely high viscosity of the fluid. Thus, we hypothesize that the instability in the 2-layer system is generated by the less viscous fluid exerting a shear stress on the viscous fluid at the interface, where there is a minimum shear stress exerted on the interface in order for destabilization to occur.

2.3.2 Influence of shaking amplitude

We first examine how varying the shaking amplitude influences the pattern features. Figure 2 shows images of the patterns for shaking amplitudes of (a-c) $A = 0.5$ cm and (d-f) $A = 1$ cm at a fixed layer height ratio of $h_w/h_t = 1$ and shaking time of 2 min. per frequency. For 1-D oscillations, the dominant pattern that forms is a

columnar structure where darker regions in the images correspond to thicker peaks in the viscous layer. By observing the side profile of the container (not shown), the peaks form pointed ridges rather than sinusoidal behavior at the interface. The column structures have noticeable imperfections: bifurcations and deviations from a straight line can occur (see Fig. 2d) for example). At fixed amplitude, increasing the oscillation frequency does not seem to change the wavelength of the columns appreciably; however, increasing shaking amplitude appears to decrease the wavelength. From the images, we estimate that the columnar pattern wavelengths are approximately 3 cm and 2 cm for $A = 0.5$ and 1 cm, respectively. Note that each of these conditions was initiated from a system at rest with the interface initially at equilibrium.

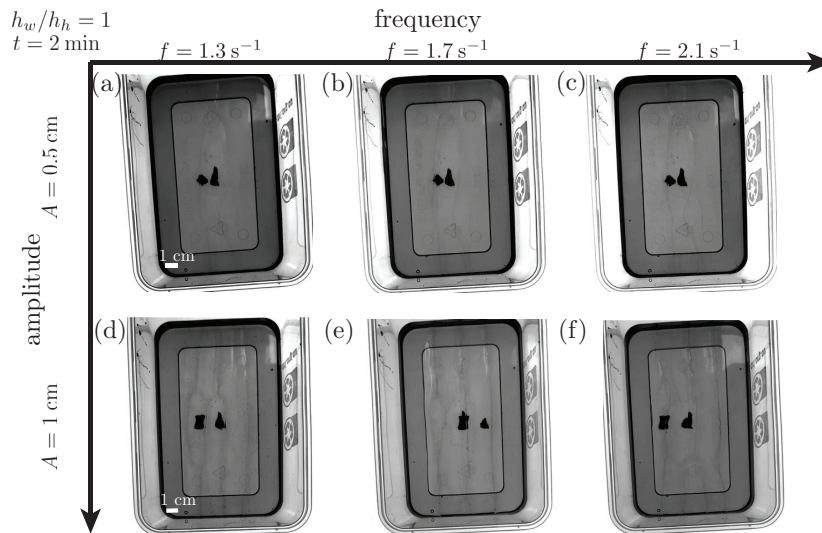


Fig. 2 Influence of amplitude on pattern formation at fixed shaking time and layer height ratio. (a-c) Shaking amplitude at 0.5 cm for increasing frequency. (d-f) Shaking amplitude at 1 cm for increasing frequency.

2.3.3 Influence of layer thickness ratio

We next vary the ratio of the layer thicknesses by tuning the thickness of the water layer and maintaining $h_h = 0.5$ cm. Figure 3 shows images of the instability patterns for varying thickness ratios ($h_w/h_h = 1/3, 2/3$ and $4/3$). For the thinnest water layer (Fig. 3(a-d)) the features of the pattern are much smaller with an approximate wavelength of 0.5–1 cm. Interestingly, as the shaking frequency increases for this layer height, the columns become more distinct (i.e. the peaks grow in height) but then seem to destabilize due to excitation by higher order modes, forming a honeycomb-

like pattern in Fig. 3(d). Increasing the thickness of the water layer produces an increase in the pattern wavelength. For $h_w/h_h = 2/3$, the wavelength is approximately 1–2 cm, and for $h_w/h_h = 4/3$, the wavelength is approximately 3–4 cm. The height of the peaks increases as well, which can be distinguished by the increased contrast difference between the peaks and the thinner fluid areas. Similarly to the varying amplitude conditions, increasing the frequency does not seem to alter the pattern wavelength.

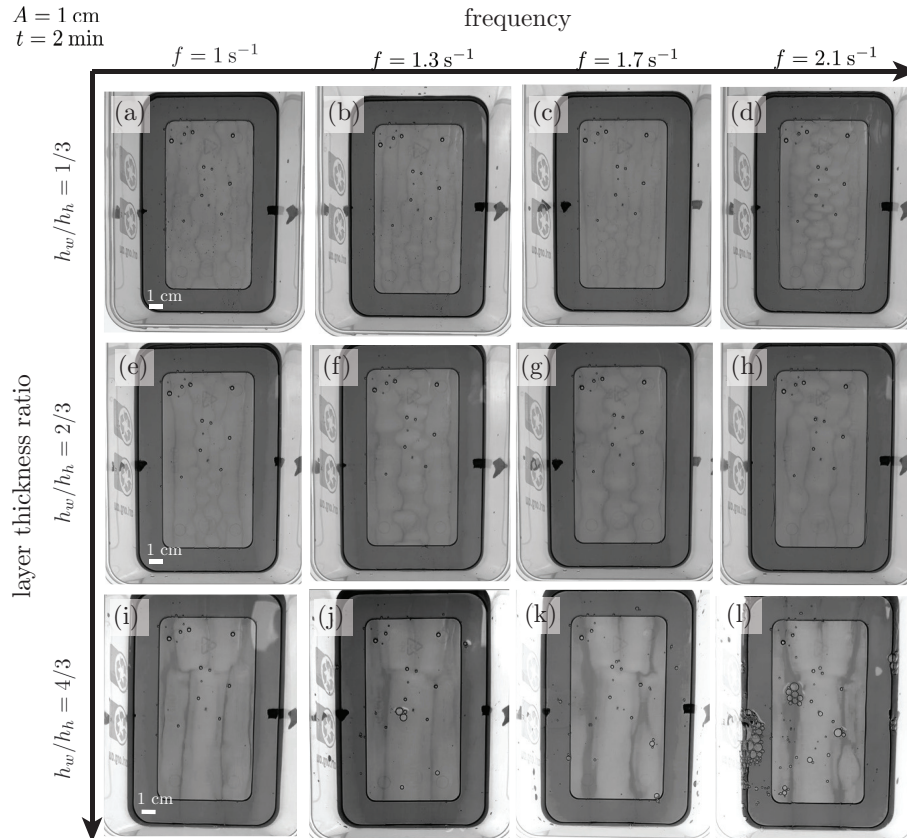


Fig. 3 Influence of layer height ratio on pattern formation at fixed shaking amplitude and shaking time. Images of patterns in syrup for water to syrup height ratios (a-d) $h_w/h_h = 1/3$, (e-h) $h_w/h_h = 2/3$, and (i-l) $h_w/h_h = 4/3$ with increasing shaking frequency. Thinner water layers (less viscous fluid) produce finer-scale patterns in the syrup.

2.3.4 Estimate of shear stress exerted on high viscosity bottom layer

The analytical solution for the base case to the exact flow set-up has been determined by Uddin and Murad [13] and the linear stability for the finite layer Stokes 2nd problem has been performed by Yih [16]; however, the time dependence and boundary conditions complicates the linear stability analysis for our system. Due to the large viscosity contrast between the fluid layers, we can consider the honey problem as an analog of Stokes second problem for an oscillating plane in a semi-infinite domain of fluid, treating the honey layer as a nearly rigid material oscillating with the bottom plate relative to flow generated in the water layer at the top. As a crude approximation for the shear stress exerted by the water on the viscous layer, we use the analytical flow field solution for Stokes second problem in the semi-infinite domain:

$$u(z, t) = U_0 e^{\sqrt{\frac{\omega}{2\nu}}z} \cos\left(\omega t - \sqrt{\frac{\omega}{2\nu}}z\right), \quad (1)$$

where U_0 is the maximum forcing speed, ν is the fluid kinematic viscosity, and ω is the oscillation frequency. The shear stress at the surface of the honey then follows:

$$\sigma|_{z=h_1} = \sqrt{\rho\omega\mu}U_0 \cos(\omega t - \pi/4). \quad (2)$$

The maximum shear stress occurring during the oscillation cycle is thus $\sigma|_{z=h_1} = \sqrt{\rho\omega\mu}U_0$. This solution is exact for a semi-infinite domain; the actual shear stress in our system will be a function of the water height depth. Here, we use this analytical expression for the shear stress to estimate an approximate maximum shear stress value generated in the experiments. Evaluating for water properties at 20°C and using the highest frequency experimental condition, we find a maximum shear stress value of roughly 0.5 Pa in our experiments.

2.3.5 Transient dynamics of pattern formation

All of the previous conditions tested so far have commenced shaking the system from rest; however, what happens when the frequency of shaking is changed transiently without allowing the system to return to equilibrium? To test this, we perform experiments by applying step changes and either ramping up or ramping down the frequency at time intervals of 2 minutes. Figure 4(a-c) shows a time series of images for the same frequency, $f = 1 \text{ s}^{-1}$, where changes in the pattern morphology over time are evident. Thus, the instability has some formation timescale that appears to decrease with increasing oscillation frequency.

Figure 4(d-g) presents images taken at the end of each interval for each frequency in the ramp up scheme. The instability pattern changes noticeably: the column wavelength increases from roughly 1 cm to 3 cm, and the peak height increases with increasing frequency (noted by the increasing contrast between the peaks and troughs). In contrast, the images in Fig. 4(h-k) show that the pattern seems to be consistent with decreasing oscillation frequency. The column wavelength seems to

be constant at roughly 2-3 cm, and the major change is a reduction in peak height with decreasing frequency. Accordingly, initializing the shaking from rest with high-frequency oscillations may “lock in” a preferred pattern in the ramp down protocol, whereas the patterns in ramping up schemes may be “overwritten” by higher frequency dynamics. Future experiments should examine longer and/or shorter time intervals at each step to determine if the patterns are indeed stable over time.

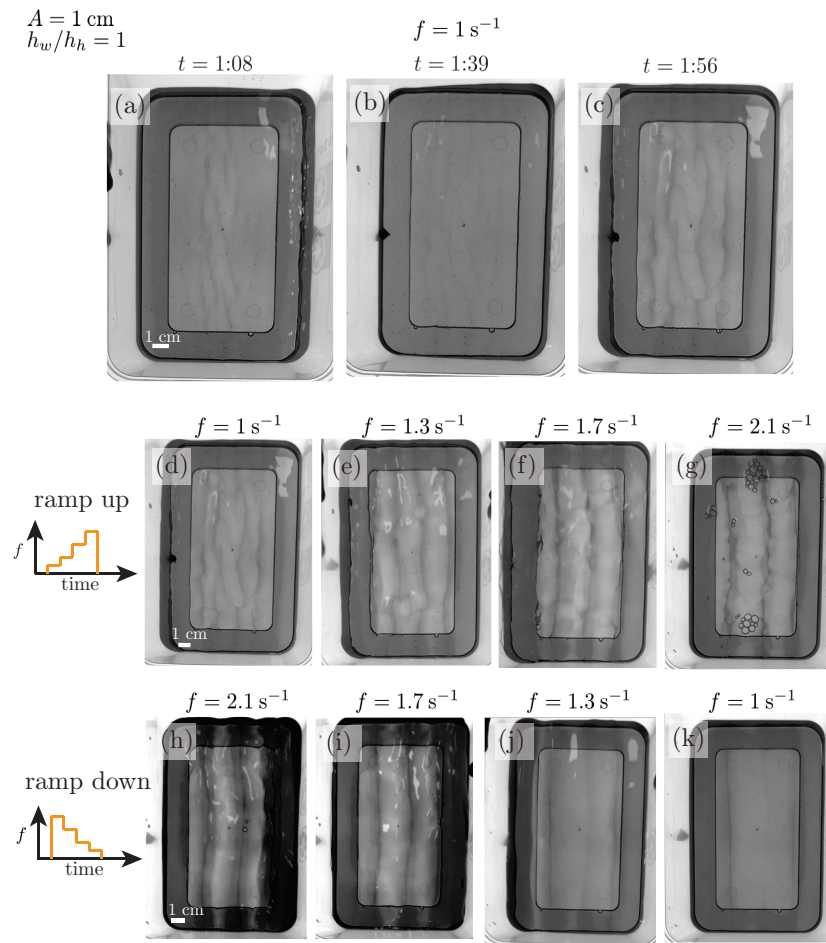


Fig. 4 Transient dynamics in pattern formation. (a-c) Time sequence of images showing the pattern development for shaking at $f = 1 \text{ s}^{-1}$, $A = 1 \text{ cm}$, and $h_w/h_h = 1$. (d-g) Stepwise ramp up in shaking frequency with 2 minutes of shaking at each frequency. (h-k) Stepwise ramp down in shaking frequency with 2 minutes of shaking at each frequency. Images are extracted from the end of each 2-minute interval.

2.3.6 Immiscible case: golden syrup and vegetable oil

We also examine the immiscible system of golden syrup and vegetable oil ($\mu = 0.05 \text{ Pa s}$, $\rho = 908 \text{ kg/m}^3$), which has a viscosity ratio of $\eta_o/\eta_w = 6 \times 10^{-4}$. Over the experimentally-tested frequencies ($f = 1\text{--}2.1 \text{ s}^{-1}$), we do not observe any visible instability formation. However, shaking arbitrarily at higher frequencies shows that an instability will develop, suggesting that lower viscosity contrast systems require larger forcing for the top layer to generate sufficient shear stress to destabilize the viscous fluid at the interface.

2.4 Experimental conclusions and discussion

Figure 5 presents a summary of the experimental test conditions probed in this work on a phase space diagram parameterized by the shaking frequency f and layer thickness ratio h_w/h_h . For the case of $h_w/h_h = 1$, we have examined two amplitude cases: $A = 0.5$ and 1 cm . We find that each of these parameters influences features of the instability pattern:

1. decreasing amplitude at fixed frequency and layer height ratio increases the pattern wavelength.
2. increasing frequency at fixed amplitude and layer height ratio increases the height of the peaks with minimal influence on pattern wavelength.
3. decreasing the thickness of the less viscous top layer relative to the viscous layer at fixed amplitude and frequency produces finer scale patterns of smaller wavelength that are more prone to destabilization by higher order modes.

The experimental results—although largely qualitative—provide some insight as to the physical mechanism driving the instability formation in viscosity-stratified fluids. Improvements to the experimental protocol include a more standardized and

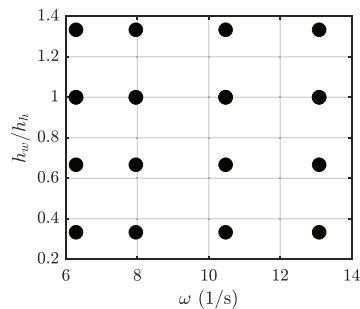


Fig. 5 Summary of experimental test conditions: parameter space comprised of frequency f and layer thickness ratio, h_w/h_h .

controlled oscillation procedure, increasing the container size to minimize the influence of wall effects, and improving the imaging set-up to enable quantitative extraction of pattern features from image processing. On the timescale of each shaking experiment, we do not anticipate that miscibility plays a large role in the instability formation; however, future work should verify this assumption using immiscible fluids. Additionally, future experiments should probe a wider range of the parameter space as well as vary the viscosity ratio more broadly to develop an improved understanding of the instability dependence on the imposed flow parameters.

3 Constant shear on a single layer of viscous fluid

We continue our investigation by building a mathematical model to further understand these instabilities. The experiments can be modeled by considering two layers of fluid of different viscosities undergoing oscillatory motion. This problem has been widely studied and notable work includes Yih's 1968 paper modeling the stability of the two-layer problem between two plates [16]. Their analysis showed that instability occurs for both Couette and Poiseuille flows. This extends the work from their 1967 paper on a single viscous layer with a free boundary undergoing oscillatory motion [15]. They showed that instability can occur for long wavelengths.

In this section we build a simplified analogous model inspired by the results of the single-layer experiments in Sect. 2.3.1. The oscillated single layer of golden syrup shows no visible surface deformation. We reason that the pattern formation arises due to the second layer and that the impact of the water layer can be interpreted as a shear force on the free surface of the golden syrup. We restrict our analysis by only considering the honey layer which displays clear instability in the experiments. We further simplify our model by analyzing the case where we have a constant and unidirectional shear stress τ at the free boundary $z = h$, as shown in Fig. 6.

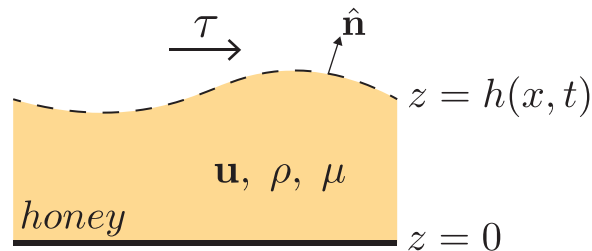


Fig. 6 Schematics of the mathematical model used to analyze the instability of a two-dimensional honey layer undergoing a constant shear stress τ in the x -direction. The layer has viscosity μ , density ρ and velocity \mathbf{u} . The free surface $z = h$ has normal $\hat{\mathbf{n}}$.

We model the two-dimensional viscous fluid layer of thickness h using the continuity and the Navier-Stokes equations:

$$\nabla \cdot \mathbf{u} = 0 \quad (3)$$

$$\rho \left(\frac{\partial \mathbf{u}}{\partial t} + \mathbf{u} \cdot \nabla \mathbf{u} \right) = -\nabla p - \rho \mathbf{g} + \mu \nabla^2 \mathbf{u} \quad (4)$$

The fluid has viscosity μ , density ρ and velocity $\mathbf{u} = (u, w)$ and where \mathbf{g} represents gravity acting in the z -direction.

3.1 Boundary conditions

At the bottom surface, the no-slip and no-flux boundary condition is applied such that

$$\mathbf{u} = 0 \quad \text{at} \quad z = 0. \quad (5)$$

The kinematic boundary condition on the free surface is expressed as

$$w = h_t + uh_x \quad \text{at} \quad z = h(x, t). \quad (6)$$

The stress boundary conditions on the free surface are chosen as follows. The force acting on the free surface \mathbf{F} at $z = h$ is defined as

$$\mathbf{F} = \underline{\underline{\boldsymbol{\sigma}}} \cdot \mathbf{n}$$

where

$$\underline{\underline{\boldsymbol{\sigma}}} = -p \underline{\underline{\mathbf{I}}} + 2\mu \underline{\underline{\mathbf{E}}} \quad (7)$$

and

$$\underline{\underline{\mathbf{E}}} = \frac{1}{2} \begin{pmatrix} 2u_x & u_z + w_x \\ u_z + w_x & 2w_z \end{pmatrix}$$

where $\underline{\underline{\mathbf{E}}}$ is the strain rate tensor, p is the pressure and $\underline{\underline{\mathbf{I}}}$ the identity matrix.

Using the continuity equation, Eq. (7) becomes

$$\underline{\underline{\boldsymbol{\sigma}}} = \begin{pmatrix} -p + 2\mu u_x & u_z + w_x \\ u_z + w_x & -p - 2\mu u_z \end{pmatrix}. \quad (8)$$

The stress in the normal direction on the free surface is therefore

$$\mathbf{F} \cdot \mathbf{n} = \gamma (\nabla \cdot \mathbf{n}) \quad (9)$$

where γ is the surface tension, \mathbf{n} is the normal vector at the surface and $\nabla \cdot \mathbf{n}$ models the local curvature of the interface. The normal vector is defined as

$$\mathbf{n} = \frac{\nabla(z-h)}{|\nabla(z-h)|} = \frac{1}{1+h_x^2} \begin{pmatrix} -h_x \\ 1 \end{pmatrix}. \quad (10)$$

By analyzing the experimental results, we reason that the surface tension should only impact short wavelengths. This is due to the capillary length being much shorter than the wavelengths of the instability. As such, the effects of surface tension are neglected and the normal stress boundary condition simplifies to

$$\mathbf{F} \cdot \mathbf{n} = 0. \quad (11)$$

The tangential stress condition is expressed as

$$\mathbf{F} \times \mathbf{n} = \boldsymbol{\tau} \quad (12)$$

where τ is the constant shear stress applied to the top boundary.

3.2 Non-dimensional model

We make the following substitutions to non-dimensionalize our equations:

$$t = \frac{\rho h_0^2}{\mu} \hat{t}, \quad x = \frac{\rho g h_0}{\tau} \hat{x}, \quad z = h_0 \hat{z}, \quad u = \frac{h_0 \tau}{\mu} \hat{u}, \quad w = \frac{\tau^2}{\rho g \mu} \hat{w}, \quad p = \rho g h_0 \hat{p},$$

where h_0 is the height of the unperturbed free surface. Dropping the $\hat{\cdot}$, the equations of motion (3) and (4) become

$$\nabla \cdot \mathbf{u} = 0, \quad (13)$$

$$u_t + \lambda(uu_x + wu_z) = -p_x + \Gamma u_{xx} + u_{zz}, \quad (14)$$

$$\Gamma w_t + \lambda \Gamma (uw_x + ww_z) = -p_z - 1 + \Gamma(\Gamma w_{xx} + w_{zz}) \quad (15)$$

where subscript t , x and z denote the partial differentials in terms of t , x and z , respectively. The dimensionless parameters are defined as

$$\Gamma = \frac{\tau^2}{\rho^2 g^2 h_0^2}$$

and

$$\lambda = \frac{h_0 \tau^2}{\mu^2 g}.$$

It is worth noting that the Reynolds number is $\text{Re} = \lambda / \sqrt{\Gamma}$.

From the experimental results, we can find the corresponding Γ and λ . For golden syrup, we use the values from Sect. 2.2.1 and choose the height of the layer to be $h_0 = 0.005$ m. To find the shear stress τ , we use Stokes' second problem for an oscillating plate which states that the maximum shear stress on the surface of the golden syrup must be

$$\tau = \rho_w u_{0,w} \omega h_w$$

where ρ_w is the density of the upper layer, which in our case is water, u_{0w} is the velocity of the upper layer, h_w the height of the upper layer and ω the frequency of the oscillations. From this expression we find that $\Gamma \approx 5 \times 10^{-5}$ and $\lambda \approx 2 \times 10^{-8}$. Since λ is small, we neglect nonlinear inertia and (14) and (15) become

$$u_t = -p_x + \Gamma u_{xx} + u_{zz}, \quad (16)$$

$$\Gamma w_t = -p_z - 1 + \Gamma(\Gamma w_{xx} + w_{zz}). \quad (17)$$

3.2.1 Non-dimensional boundary conditions

The boundary conditions (5) at the bottom plate $z = 0$ become

$$u = 0 \quad \text{at} \quad z = 0, \quad (18)$$

$$w = 0 \quad \text{at} \quad z = 0. \quad (19)$$

At the free surface the boundary conditions (6, 11, 12) become

$$\lambda w = h_t + \lambda u h_x, \quad (20)$$

$$\left(\frac{1}{1 + \Gamma h_x^2} \right) (-4\Gamma u_x h_x + (1 - \Gamma h_x^2)(u_z + \Gamma w_x)) = 1, \quad (21)$$

$$\Gamma h_x^2(-p + 2\Gamma u_x) - p - 2\Gamma u_x - 2\Gamma h_x(u_z + \Gamma w_x) = 0, \quad (22)$$

respectively.

3.3 Base state solution

The simple base state of this model can be found by assuming that the fluid flow is steady and the velocity is independent of the x -direction:

$$\mathbf{u}(z) = u(z)\mathbf{i} + w(z)\mathbf{k}$$

The free surface is unperturbed and sits at $z = h_0$ where h_0 is constant. Non-dimensionally this is given by $z = 1$.

The boundary conditions simplify to

$$u = 0 \quad \text{at} \quad z = 0, \quad (23)$$

$$w = 0 \quad \text{at} \quad z = 0, 1, \quad (24)$$

$$u_z = 1 \quad \text{at} \quad z = 1, \quad (25)$$

$$p = 0 \quad \text{at} \quad z = 1, \quad (26)$$

$$(27)$$

and the continuity equation becomes $w_z = 0$. As such, the velocity in the vertical direction is $w = 0$. The Navier-Stokes equations (16) and (17) simplify to

$$0 = u_{zz}, \quad (28)$$

$$p_z = -1, \quad (29)$$

which can easily be solved to find that

$$\begin{aligned} u &= z, \\ p &= 1 - z. \end{aligned} \quad (30)$$

In the base case, the fluid velocity is only in the direction of the shear stress and the pressure is hydrostatic.

3.4 Linear perturbation

To investigate the instabilities seen in the experiments we perturb our base state with the following linear expansions:

$$u = u_0 + \varepsilon u_1 + \varepsilon^2 u_2 + \dots, \quad (31)$$

$$w = \varepsilon w_1 + \dots, \quad (32)$$

$$h = 1 + \varepsilon h_1 + \dots, \quad (33)$$

$$P = P_0 + \varepsilon P_1 + \dots \quad (34)$$

Substituting (30), this simplifies to

$$u = z + \varepsilon u_1, \quad (35)$$

$$w = \varepsilon w_1, \quad (36)$$

$$h = 1 + \varepsilon h_1, \quad (37)$$

$$P = 1 - z + \varepsilon P_1, \quad (38)$$

up to order ε .

The Navier-Stokes equations (16) and (17) can now be evaluated at order ε to give

$$u_{1t} = -p_{1x} + \Gamma u_{1xx} + u_{1zz}, \quad (39)$$

$$\Gamma w_{1t} = -p_{1z} + \Gamma(\Gamma w_{1xz} + w_{1zz}). \quad (40)$$

Furthermore, the continuity equation at order ε allow us to introduce a stream function $\psi(x, z, t)$ such that

$$u_1 = \psi_z, \quad (41)$$

$$w_1 = -\psi_x, \quad (42)$$

and we define the perturbations to be

$$\psi(x, z, t) = f(z)e^{\sigma t + ikx},$$

$$P_1 = g(z)e^{\sigma t + ikx},$$

$$h_1 = Ae^{\sigma t + ikx},$$

where σ is the growth rate of our perturbation, k the wave number, A is a constant, and f and g are functions of z which are yet to be determined.

Substituting the ansatz into Eqs. (39) and (40) gives

$$\sigma f' = -ikg + f''' - k^2\Gamma f' \quad (43)$$

$$-ik\sigma\Gamma f = -g' - \Gamma(ikf'' - ik^3\Gamma f). \quad (44)$$

These can be reduced to a linear ODE for $f(z)$ by differentiating (43) with respect to z and multiplying (44) by $-ik$ and adding the resulting equations together. This gives

$$f'''' + (-2k^2\Gamma - \sigma)f'' + (k^4\Gamma + k^2\sigma\Gamma)f = 0, \quad (45)$$

where $'$ denotes a differential in terms of z . The general solution of (45) is

$$f = \alpha_1 \cosh m_1 z + \alpha_2 \cosh m_3 z + \alpha_3 \sinh m_1 z + \alpha_4 \sinh m_3 z, \quad (46)$$

where $\alpha_1, \alpha_2, \alpha_3, \alpha_4$ are 4 unknowns and

$$m_1 = \sqrt{k^2\Gamma} \quad \text{and} \quad m_3 = \sqrt{k^2\Gamma + \sigma}.$$

3.4.1 Boundary conditions

Similarly, we perturb the boundary conditions by substituting (35)–(38). The no-slip boundary condition remains as

$$u_1 = w_1 = 0 \quad \text{at} \quad z = 0.$$

At the free surface $z = 1 + \varepsilon h_1 + \dots$, we further Taylor expand about $z = 1$ to obtain

$$\lambda w_1 = h_{1z} + \lambda u_0 h_{1x} \quad \text{at} \quad z = 1, \quad (47)$$

$$u_{1z} + \Gamma w_{1x} = 1 \quad \text{at} \quad z = 1, \quad (48)$$

$$h_1 - p_1 - 2\Gamma(u_{1x} + h_{1x}) = 0 \quad \text{at} \quad z = 1 \quad (49)$$

for the kinematic, tangential and normal stress at order ε , respectively.

Further substitutions from the respective ansatz into our boundary conditions gives

$$f(0) = 0, \quad (50)$$

$$f'(0) = 0, \quad (51)$$

$$-ik\lambda f(1) = \sigma A + ik\lambda A, \quad (52)$$

$$f''(1) + k^2\Gamma f(1) = 0, \quad (53)$$

$$A - g(1) - 2\Gamma(ikf'(1) + ikA) = 0. \quad (54)$$

3.4.2 Finding the solution at order ε

We use the kinematic boundary condition (52) to eliminate the constant A from the normal stress condition (54). We also eliminate the function g in (54) by evaluating equation (43) at $z = 1$. This simplifies our boundary conditions to

$$f(0) = 0, \quad (55)$$

$$f'(0) = 0, \quad (56)$$

$$f''(1) + k^2\Gamma f(1) = 0, \quad (57)$$

$$(\lambda k^2 - 2ik^3\Gamma\lambda)f + (\sigma + ik\lambda)((\sigma + 3k^2\Gamma)f'(1) - f'''(1)) = 0. \quad (58)$$

By using the boundary conditions at $z = 0$, we deduce that (46) must simplify to the form

$$f(z) = \alpha_1(\cosh m_1 z - \cosh m_3 z) + \alpha_3 \left(\sinh m_1 z - \frac{m_1}{m_3} \sinh m_3 z \right). \quad (59)$$

The final two boundary conditions (57) and (58) can be used to determine the last two unknowns α_1 and α_3 such that

$$\begin{pmatrix} A_{11} & A_{12} \\ A_{21} & A_{22} \end{pmatrix} \begin{bmatrix} \alpha_1 \\ \alpha_3 \end{bmatrix} = 0 \quad (60)$$

where

$$\begin{aligned} A_{11} &= \cosh m_1(m_1^2 + k^2\Gamma) - \cosh m_3(m_3^2 + k^2\Gamma), \\ A_{12} &= \sinh m_1(m_1^2 + k^2\Gamma) - \sinh m_3(m_1 m_3 + k^2 \frac{m_1}{m_3} \Gamma), \\ A_{21} &= (k^2\lambda - 2ik^3\lambda\Gamma)(\cosh m_1 - \cosh m_3)\dots \\ &\quad + (\sigma + ik\lambda)(\sigma + 3k^2\Gamma)(m_1 \sinh m_1 - m_3 \sinh m_3)\dots \\ &\quad - (\sigma + ik\lambda)(m_1^3 \sinh m_1 - m_3^3 \sinh m_3), \\ A_{22} &= (k^2\lambda - 2ik^3\lambda\Gamma)(\sinh m_1 - \frac{m_1}{m_3} \sinh m_3)\dots \\ &\quad + (\sigma + ik\lambda)(\sigma + 3k^2\Gamma)(m_1 \cosh m_1 - m_1 \cosh m_3)\dots \\ &\quad - (\sigma + ik\lambda)(m_1^3 \cosh m_1 - m_1 m_3^2 \cosh m_3), \end{aligned}$$

and a non-trivial solution of $f(z)$ requires that the determinant of the matrix in (60) is zero.

Furthermore, $\det(A) = 0$ provides a relationship between the growth rate σ and the wave number k which can be used to investigate the stability of our model. By using the experimental values for Γ and λ found in Sect. 3.2, we can find non-trivial solutions of σ for each wave number. This was done using a code in MATLAB and plotting the position of the minimum absolute value of the determinant $\det(A)$ for inputs of σ and k .

At these minimums, focusing on the real part of σ allows us to find the wavelengths at which the model is unstable. This would require $Re(\sigma) > 0$. As shown in Fig. 7, $Re(\sigma)$ is always negative for all wave numbers and therefore the system is stable.

We also investigated other systems by increasing the values of Γ and λ up to $\Gamma = \lambda = 1$ and found that all led to negative $Re(\sigma)$ values for non-trivial wave numbers. Therefore, we conclude that a viscous layer under constant unidirectional shear stress is stable. To investigate the instability seen in the experiments, further aspects need to be incorporated into the model. For example, the viscosity difference of the second layer or the change in the direction of the shear stress from the oscillations.

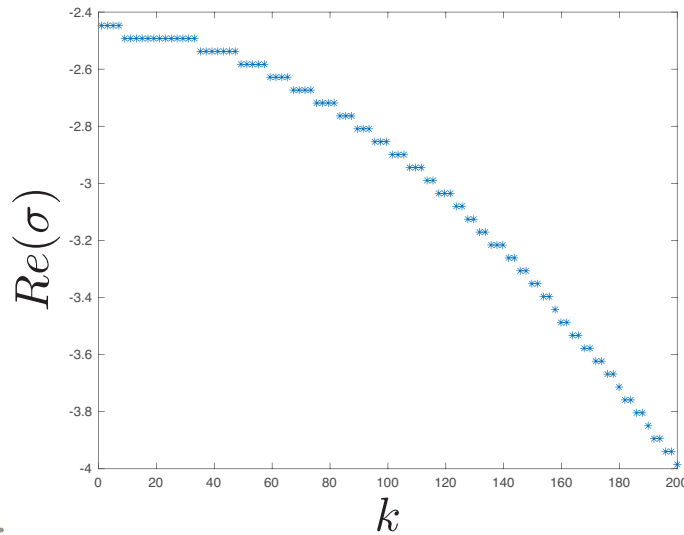


Fig. 7 Plot of the non-trivial real part of the growth rate σ against discrete values of the wave number k for the perturbations associated with the experimental values from Sect. 3.2.

Acknowledgements We would like to acknowledge the invaluable guidance of Dr Edward Hinton and A/Prof. Duncan Hewitt with the mathematical model, A/Prof. Anja Slim for providing us with the necessary experimental equipment, Dr Michael Dallaston for his coding expertise and Dr Draga Pihler-Puzović for coming up with the problem. We would also like to extend our thanks to the MATRIX Institute for hosting the workshop on instabilities of fluid flow in porous media.

References

1. Amin, M.S., Elborai, S., Lee, S.H., He, X., Zahn, M.: Surface tension measurement techniques of magnetic fluids at an interface between different fluids using perpendicular field instability. *J. Appl. Phys.* **97**(10) (2005). DOI 10.1063/1.1861374
2. Bagnold, R.A.: Motion of waves in shallow water. Interaction between waves and sand bottoms. *Proc. R. Soc. Lond. A* **187**(1008), 1–18 (1946). DOI 10.1098/rspa.1946.0062
3. Blondeaux, P.: Sand ripples under sea waves Part 1. Ripple formation. *J. Fluid Mech.* **218** (1990). DOI 10.1017/S0022112090000908
4. Govindarajan, R., Sahu, K.C.: Instabilities in Viscosity-Stratified Flow. *Annu. Rev. Fluid Mech.* **46**(1), 331–353 (2014). DOI 10.1146/annurev-fluid-010313-141351
5. Hinch, E.J.: A note on the mechanism of the instability at the interface between two shearing fluids. *J. Fluid Mech.* **144**, 463–465 (1984). DOI 10.1017/S0022112084001695
6. Hooper, A.P.: Long-wave instability at the interface between two viscous fluids: Thin layer effects. *The Physics of Fluids* **28**(6), 1613–1618 (1985). DOI 10.1063/1.864952

7. Hooper, A.P., Boyd, W.G.C.: Shear-flow instability at the interface between two viscous fluids. *J. Fluid Mech.* **128**, 507 (1983). DOI 10.1017/S0022112083000580
8. Li, C.H.: Instability of Three-Layer Viscous Stratified Flow. *Phys. Fluids* (1969)
9. Lin, S.P.: Instability of a Liquid Film Flowing down an Inclined Plane. *Phys. Fluids* **10**(2), 308–313 (1967). DOI 10.1063/1.1762110
10. Perron, J.T., Myrow, P.M., Huppert, K.L., Koss, A.R., Wickert, A.D.: Ancient record of changing flows from wave ripple defects. *Geology* **46**(10), 875–878 (2018). DOI 10.1130/G45463.1
11. Renardy, Y.: Instabilities in steady flows of two fluids. *Rocky Mountain J. Math.* **18**(2) (1988). DOI 10.1216/RMJ-1988-18-2-455
12. Talib, E., Jalikop, S.V., Juel, A.: The influence of viscosity on the frozen wave instability: theory and experiment. *J. Fluid Mech.* **584**, 45–68 (2007). DOI 10.1017/S0022112007006283
13. Uddin, M., Murad, A.: Stokes' second problem and oscillatory Couette flow for a two-layer fluid: Analytical solutions. *Alexandria Engineering Journal* **61**(12), 10,197–10,218 (2022). DOI 10.1016/j.aej.2022.03.023
14. Westra, M.T., Binks, D.J., Van De Water, W.: Patterns of Faraday waves. *J. Fluid Mech.* **496**, 1–32 (2003). DOI 10.1017/S0022112003005895
15. Yih, C.S.: Instability due to viscosity stratification. *J. Fluid Mech.* **27**(2), 337–352 (1967). DOI 10.1017/S0022112067000357
16. Yih, C.S.: Instability of unsteady flows or configurations Part 1. Instability of a horizontal liquid layer on an oscillating plane. *J. Fluid Mech.* **31**(4), 737–751 (1968). DOI 10.1017/S0022112068000443